Mousavi, S. M., Kamali, R., Sotoudeh, F., Karimi, N. and Khojasteh, D. (2019) Large eddy simulation of pseudo shock structure in a convergent-long divergent duct. *Computers and Mathematics with Applications*, (doi: 10.1016/j.camwa.2019.10.017)

There may be differences between this version and the published version. You are advised to consult the publisher's version if you wish to cite from it.

http://eprints.gla.ac.uk/201330/

Deposited on 1 November 2019

Enlighten – Research publications by members of the University of Glasgow
http://eprints.gla.ac.uk

Large Eddy Simulation of Pseudo Shock Structure in a Convergent-Long Divergent Duct

Seyed Mahmood Mousavi[1*], Reza Kamali[1], Freshteh Sotoudeh[1], Nader Karimi[2], Danial Khojasteh[1, 3]

[1]School of Mechanical Engineering, Shiraz University, Shiraz 71936-16548, Iran

[2]School of Engineering, University of Glasgow, Glasgow G12 8QQ, United Kingdom

[3]Water Research Laboratory, School of Civil and Environmental Engineering, UNSW Sydney, NSW, Australia

Abstract

In this paper, the Pseudo shock structure in a convergent-long divergent duct is investigated using large eddy simulation on the basis of Smagorinsky-Lilly, Wall-Adapting Local Eddy-Viscosity and Algebraic Wall-Modeled LES subgrid models. The first objective of the study is to apply different subgrid models to predict the structure of Lambda form shocks system, while the ultimate aim is to obtain further control of the shock behavior. To achieve these goals, the dynamic grid adaption and hybrid initialization techniques are applied under the 3D investigation to reduce numerical errors and computational costs. The results are compared to the existing experimental data and it is found that the WMLES subgrid model results in more accurate predictions when compared to the other subgrid models. Subsequently, the influences of the divergent section length with the constant ratio of the outlet to throat area and, the effects of discontinuity of the wall temperature on the flow physics are investigated. The results indicate that the structure of compressible flow in the duct is affected by varying these parameters. This is then further discussed to provide a deeper physical understanding of the mechanism of Pseudo shock motion.

Keywords: Pseudo shock system; compressible LES; subgrid model; Lambda shock structure.

[*] Corresponding author; Email address: sm.mousvi@shirazu.ac.ir

Nomenclature			Greek letters		
d_w	Wall distance	m	δ	Kronecker delta	-
h	enthalpy	J	Δ	local grid scale	-
L_s	mixing length for subgrid scale strain rate	m	ε_t	sub-grid scale dissipation	m^2/s^3
u	velocity vector	m/s	μ_t	eddy-viscosity	Pa.s
p	pressure	Pa	ρ	density	kg/m^3
P_{rt}	Turbulent Prandtl number	-	τ_{ij}	stress tensor	Pa
S_{ct}	Turbulent Schmidt number	-	Symbols		
S_{ij}	rate-of strain tensor	1/s	$\sim$	filtered Faver	-
V	velocity	m/s	$\bar{}$	filtered quantities	-

1. Introduction

Interactions among shock waves, boundary layer, and flow separation are important phenomena in modern high speed aerodynamics [1]. These phenomena are key elements in designing the propulsion systems in which long ducts are considered as integral parts [2]. The length of a duct is typically obtained by using empirical correlations based on the maximum pressure rising between the inlet and the exit of the duct [3]. Recently, various experimental and numerical investigations have been conducted to better understand the pseudo shock system. For example, Xu et al. [4] reported that the effect of background waves on the growth of separation flow plays a principal role in the jump characteristic of the shock train leading edge. Li et al. [5] investigated the path of shock train leading edge in complex background waves and reported a mathematical model for the path. Zhang et al. [6] classified the shock train using the pressure distribution or shock train location. Mousavi et al. [7] found that the changes in ramp dimension as a passive control method and wall temperature as an active control method could change the shock waves characteristics r and the length of the Lambda shock systems. Wang et al. [8] reported that the

behaviors of unsteady oblique shock train and boundary layer interactions are related to the dynamics of shock motion. The effects of cavity depth on shock train structure was studied by Kumar and Vaidyanathan [9] who showed that the strength of the shock train system decreases with an increase in the depth of the cavity. Su et al. [10] controlled the pseudo-shock oscillation in a scramjet inlet-isolator by applying periodical excitation. Vanstone et al. [11, 12] proposed a simple physics-based model for the prediction of shock-train location. Shi et al. [13] compared the shock train behavior under sinusoidal and constant backpressure and they found that the oscillations in shock train move downstream of the flow. The incident shocks effects on close-loop control (CLC) of the shock train location are experimentally studied by Li et al. [14] who found that it makes the CLC unstable.

Using the numerical methods is an appropriate way to study the flow structure in complex conditions [15-17]. Computational fluid dynamics (CFD) [18], based on Reynolds-averaged Navier–Stokes (RANS) equations, is a potential tool to investigate the flow behavior in an isolator. Using this tool, Rockwell et al. [19] controlled the shock train structure with a characteristic model based All-Coefficient Adaptive Control approach. Nonetheless, accuracy of RANS methodology is limited when facing the complex shock wave-boundary layer interactions. Over the past decade, large-eddy simulation (LES) has emerged as a promising alternative for prediction of turbulent flows behavior. This methodology is currently being applied to a wide variety of engineering applications, including combustion [20-27], simulations of the wind turbine [28], acoustics [29-32], combustion noise [33, 34] and several studies of SBLI [35, 36]. To illustrate, Koo and Raman [37] applied the dynamic Smagorinsky subgrid model for supersonic inlet of an isolator and they found that this model is suitable for capturing the large-scale features of the unstart process. Vane et al. [38] indicated that the accuracy of the Wall-Modeled LES (WMLES) subgrid model is more

than Wall-Resolved LES to predict the turbulent boundary layer interacting with a shock train system in a duct with constant area. The ability of LES methodology to predict the behavior of corner vortices and recirculation zones for a pseudo-shock waves in a Laval nozzle was presented by Quaatz et al. [39]. Morgan et al. [40] investigated the normal shock train in a constant area isolator using LES methodology. They showed the potential of LES to observe the pertinent physical phenomena such as lack of reversed flow in the mean and the development of secondary shear layers. Using LES and RANS methodologies, Mousavi et al. [41-43] showed that variations in the heat generation rate and the total temperature of air flow affect the starting point of Lambda shocks system and its strength, the minimum pressure and the maximum flow Mach number. In another work, they [44] analyzed effects of the inlet total pressure, back pressure, nozzle inlet angle and wall temperature on the behavior of the shock train system. Using the same method, Goshtasbi-rad and Mousavi [45] reported that the local changes in wall temperature, free stream Reynolds number and total pressure affect the reattached shock waves as well as the collision angle of separated shock waves. Mahapatra et al. [46] observed the accurate mixing region of pseudo shock waves system in turbulent diffuser in supersonic condition using an explicit LES methodology. Using RANS model and LES methodology, the shock train structure, separation characteristics and Mach number distribution were analyzed by Joy et al. [47] by observing the back and forth movement of the shock train.

From the above discussions, it is clear that there are several works on understanding the shock train structure in various working conditions. However, because of the enormous applications of pseudo shock phenomenon in modern aerodynamics, this phenomenon still needs further examinations to control its behaviors under different conditions. Therefore, the main objective of the present work is to study the pseudo shock structure in a 3D convergent–long divergent duct.

To serve this purpose, a finite volume code with LES method through various subgrid scale (SGS) models, hybrid initialization and the dynamic grid adaptation techniques [48] are employed. To evaluate the accuracy of the numerical results, the root of R-square formula (RRF) is applied. After validating the accuracy of the obtained results, the length of divergent section is changed with a constant ratio of outlet to throat area to analyze the behavior of the shock system. In addition, the effect of discontinuity in wall temperature on shock structure is examined.

2. Numerical Modelling

2.1. Large Eddy Simulation

LES is a mathematical methodology for computational modelling of turbulent flows. It was first proposed by Smagorinsky [49] for simulation of atmospheric air flows, and was explored by Deardorff [50]. In LES methodology, filters are used to separate the large-scale eddies from small ones [51]. Therefore, φ as a variable is divided into grid and subgrid parts. By filtering compressible Navier-stokes equations, the following filtered equations are generated.

$$\frac{\partial \bar{\rho}}{\partial t} + \frac{\partial}{\partial x_i} \cdot \left(\rho \tilde{u}_i \right) = 0 \tag{1}$$

$$\frac{\partial \bar{\rho} \tilde{u}_i}{\partial t} + \frac{\partial}{\partial x_i} \left(\bar{\rho} \tilde{u}_i \tilde{u}_j \right) + \frac{\partial \bar{p}}{\partial x_i} = \frac{\partial}{\partial x_i} \left(-\overline{\tau_{ij}} + \mu_{SGS} \left(\frac{\partial \tilde{u}_i}{\partial x_j} + \frac{\partial \tilde{u}_i}{\partial x_i} \right) + \frac{\delta_{ij}}{3} T_{kk} \right) \tag{2}$$

$$\frac{\partial \bar{\rho} \tilde{h}}{\partial t} + \frac{\partial}{\partial x_i} \left(\bar{\rho} \tilde{u}_i \tilde{h} \right) = \overline{\frac{Dp}{Dt}} + \frac{\partial}{\partial x_i} \left(\left(\frac{\mu}{\mathrm{Pr}} + \frac{\mu_{SGS}}{\mathrm{Pr}_t} \right) \frac{\partial \tilde{h}}{\partial x_i} \right) \tag{3}$$

The isentropic contribution, T_{kk} is unknown parameter which attracted to the filtered pressure. In addition, the subgrid scale kinetic energy is calculated from [51, 52]:

$$\frac{\partial K_{SGS}}{\partial t} + \frac{\partial \tilde{u}_j K_{SGS}}{\partial x_i} = \frac{\partial}{\partial x_i} \left(\frac{\mu_{SGS}}{\bar{\rho}\, \mathrm{Pr}_t} \frac{\partial K_{SGS}}{\partial x_i} \right) - \tau_{ij} \frac{\partial \tilde{u}_j}{\partial x_i} - \varepsilon_{SGS} \tag{4}$$

μ_{SGS} is the subgrid scale viscosity which in Smagorinsky-Lilly [49] subgrid model it is obtained from:

$$\mu_t = \rho L_s^2 \left|\bar{S}\right| \tag{5}$$

in which

$$\left|\bar{S}\right| = \sqrt{2\bar{S}_{ij}\bar{S}_{ij}}$$

in WALE [53] subgrid model, it is calculated from:

$$\mu_t = \rho L_s^2 \frac{\left(S_{ij}^d S_{ij}^d\right)^{3/2}}{\left(\bar{S}_{ij}\bar{S}_{ij}\right)^{5/2} + \left(S_{ij}^d S_{ij}^d\right)^{5/4}} \tag{6}$$

where

$$S_{ij}^d = 0.5\left(\left(g_{ij}\right)^2 + \left(g_{ji}\right)^2\right) - \frac{1}{3}\delta_{ij}\left(g_{kk}\right)^2,\ g_{ij} = \partial\bar{u}_i / \partial x_j$$

and finally in WMLES, the subgrid scale viscosity is achieved as follows [54, 55]:

$$\mu_t = \min\left[\left(0.41 d_w\right)^2, \left(0.2\Delta\right)^2\right] \cdot \rho S \cdot \left\{1 - \exp\left[-\left(y^+ / 25\right)^3\right]\right\} \tag{7}$$

2.2. Hybrid Initialization

Hybrid initialization is a useful initialization method which works with a component of instructions and boundary interpolation methods. It solves the Laplace equation to produce velocity and pressure fields as follows:

$$\nabla^2 \varphi = 0 \tag{8}$$

$$\nabla^2 P = 0 \tag{9}$$

These equations are solved with suitable boundary conditions to provide the smooth velocity and pressure fields in the computational domain. In this method, the pressure field is computed as $\pm 1\%$

of specified gauge pressure and total pressure for the outlet and inlet zones. Moreover, the velocity for the inlet boundaries is computed as follows:

$$\left.\frac{\partial \varphi}{\partial n}\right|_{inlet} = V_{\perp} \tag{10}$$

On the wall boundaries, the normal gradient of *P* and normal velocity are set to zero.

$$\left.\frac{\partial P}{\partial n}\right|_{wall} = 0 \tag{11}$$

$$\varphi = 0 \tag{12}$$

Further, the temperature is initialized with a constant value. Hence, it can be concluded that, a hybrid initialization helps reaching the final converged solution in shorter time in comparison with standard initialization approach [56].

Additionally, in order to discretize the pressure equation, we used the second order upwind scheme [57] and the central differencing scheme [58] was used for discretizing the momentum, energy and density equations. Furthermore, the boundary conditions for turbulent characteristics are presented in Table 2.

3. Boundary Conditions and Geometry Characteristics

A schematic representation of duct geometry evaluated in this study is indicated in Fig.1. This duct consists of a 50 mm converging part with 10° angle, a 600 mm diverging part and a throat with 1.5° outlet angle and 3 mm height locating at coordinates (0, 0, 0). At the convergent section, there are two 1.5°converging angles at the distances of 25 and 160 mm far away from the throat. In addition, the height of the duct at the distance of 160 mm from the throat is 8 mm. This geometry is dimensionally similar to the one used in the work of Weiss et al. [1].

The proper boundary conditions need to be introduced to run the simulations. The initial values of the inlet and outlet of the duct are chosen based on the experimental data presented in Table 1. It

can be seen that the flow enters the duct fast, while the wall temperature remains fixed. In this paper, the pressure condition is applied at the inlet in order to satisfy the velocity in accordance with the work of Weiss et al. [1]. As the boundary condition takes static and stagnation pressure, the velocity is satisfied due to isentropic relations. This is because the boundary layer does not grow in the inlet section and there is no discontinuity in the flow and thermal transfer properties in this section. It should be noted that either the static or stagnation pressure needs to be available in order to evaluate the other pressure. The stagnation pressure is 4.8 bar and the outlet pressure is 3.25 bar [1]. The working fluid is assumed to be dry air and is treated as an ideal gas. Further, the wall temperature is 300 K and the no-slip condition is used for the channel walls.

Grid independency checking has been carried out separately for each subgrid model, and it is found that the computational grid with 3.2×10^7 cells is appropriate for WMLES subgrid. Figure 2 indicates the sample cell structure of the computational domain. It should be noted that after applying the pressure gradient dynamic adaptation technique, the number of required cells changed to 5.4×10^7 cells (for WMLES).

4. Result and Discussion

4.1. Comparison of Subgrid Models

Figures 3 shows the comparison among the obtained results of three subgrid models and the experimental data reported in Ref. [1] for the time averaged Mach number in centerline of the duct and wall pressure. Evidently, for all the three subgrid models, the simulations predict the first shock position in the duct with acceptable accurately. Both WMLES and WALE subgrid models provide similar results in a distance between the beginning of the shock train and duct outlet. These subgrid models are in good agreement with the experiments data [1]. However, according to the results, the accuracy of the WMLES is more than WALE models in a way that the RRF value to

predict the wall pressure is 93 for WMLES while it is 92 for WALE model. Also, this value is 94 for WMLES at the prediction of centerline Mach number while, it is equal to 90 for WALE model with higher number of grid cells. Thereupon, the WMLES solution is more accurate and slightly performs better than the WALE model, particularly prior to the beginning of shock train system. This is because of the rapid development of boundary layer thickness over the duct wall as well as the growth of the gradient of velocity in this area. Probably, the WALE subgrid model gives a better result with finer grids near the wall which increases the computational costs. The Smagorinsky-lilly model presents slightly different results, particularly before and after the beginning of shock train system which is due to a limitation of the Smagorinsky-lilly model in wall-bounded flow [59-61]. Concerning CPU time, the Smagorinsky-lilly and WALE subgrid models need 8% to 10% more CPU time in each iteration in comparison with the WMLES model, as the number of the computational cells increased. In addition, due to a decrease in the number of cells in the WMLES model, the cost ratio in terms of computational time between the aforementioned subgrid models is around 1:3 for our current test case. It follows that for the current case of the duct shock train, WMLES subgrid model is superior to the other models. In addition, As depicted in Fig. 4, the WMLES subgrid model is able to detect the exact structure of Lambda shocks system based on the existing experimental data [1].

4.2. Unsteadiness Effects

Figures 5(a-b) and 6 show the results of WMLES subgrid model for instantaneous contours of stagnation pressure and pressure gradient at the center surface of the duct for the time period of 1.86 to 2.02 ms. Furthermore, the distribution of instantaneous centerline stagnation pressure on this period are shown in Fig. 6. The results show that the changes in the flow behavior and shock unsteadiness are insignificant. It is due to the small angle of the divergence part of the system,

which helps the flow nearly reach the steady state condition. It should be noted that similar results have been reported by Gatski and Bonnet [36].

4.3. Effect of duct length

The variations in the compressible flow behavior and structure consisting of lambda shocks series in the long duct are investigated in this section. This behavior is due to changes in the length of the diverging part of the duct and the relevant boundary conditions which are given in table 1. Five different diverging section lengths including 0.56 (α_4=1.65^o), 0.58 (α_4=1.57^o), 0.60 (α_4=1.45^o), 0.62 (α_4=1.41^o) and 0.64 m (α_4=1.37^o) are applied for this purpose, while the ratio of the outlet area to throat area remains constant. The results are illustrated in Figs. 7 to 10. According to Fig. 7, the minimum flow pressure of 0.94 bar for the diverging length of 0.56 m decreases to 0.78 bar for the diverging length of 0.64 m. Additionally, the maximum Mach number increases from 1.71 (for diverging length of 0.56 m) to 1.88 (for diverging length of 0.64 m), as indicated in Fig. 8 and table 3. A decrease in the minimum flow pressure and an increase in the maximum Mach number result in an increase in lambda shock strength due to a change in the diverging angle followed by variations in structure of the flow separation and boundary layer thickness based on Fig. 9.

The contour of pressure distribution gradient along the duct is shown in Fig. 10. Applying pressure gradient is a proper way to predict flow structure as there are severe discontinuities in the flows with shock waves. It is noted from this figure that shock wave structure is well marked using this contour. Furthermore, as the length of diverging part increases (due to a decrease in diverging angle followed by a delay in flow separation), the location of the first lambda shock wave moves towards the section of duct outlet. According to the earlier discussion, it can be deduced that in a constant outlet pressure, the shock strength increases while moving towards the duct exit as proved by [1]. The Mach number distribution is depicted in Fig. 11 to present the effects of variations in

the length of the diverging part on the distance between the first and the second lambda shocks. Since a decrease in the diverging length causes an increase in boundary layer thickness, it makes the shock wave occur faster in a duct with shorter diverging length. This fast occurrence in flow discontinuities also affects the downstream flow such that a reduction in the diverging length from 0.64 to 0.56 m leads to a decrease in the distance between the first and the second lambda shocks from 10.55 to 8.667 mm, respectively. As the shock strength is further weakened by a decrease in the diverging length, it can be deduced that the total strength of the shock system is reduced with a decrease between the shock waves distance.

4.4. Effect of discontinuity in wall temperature

In this section, the effects of discontinuity (jump) in the wall temperature on the flow structure are analyzed. Jumps in the wall temperature are applied where first lambda shock occurs with 10 mm length. The discontinuous temperatures are varied from 200 to 700 K in steps of 100 K. The applied boundary conditions are like those represented in table 1, and the wall is not set to adiabatic condition but constant temperature at the jump location. Figure 12 shows the pressure distribution over the duct wall, indicating that as the discontinuity temperature rises from 200 K to 700 K, the minimum flow pressure decreases gradually. It should be noted that in the duct diverging part, the flow structure mainly depends on the fluid viscosity, and consequently, on the boundary layer thickness. In accordance with Sutherland's law, as the discontinuity in temperature increases, the fluid viscosity rises. Hence, as shown in Fig. 13, the flow Reynolds number diminishes with an increase in temperature. Therefore, since the Reynolds number diminishes, the boundary layer thickness increases and forces the shock waves to occur earlier. Figure 14 illustrates the Mach number distribution when the temperature jump is applied at the duct's wall. It is obvious that as the wall temperature at the shock waves location occurrence increases, the maximum Mach

number decreases followed by a reduction in the shock strength. The reason of this phenomenon is the dependency of the speed of sound on temperature as well as the reverse relation between the Mach number and the flow temperature. A rise in the flow temperature causes an increase in the speed of the sound and leads to a decrease in flow Mach number. In addition, a decrease in the flow maximum Mach number for a fixed geometry and constant pressure results in declining shock wave strength. Therefore, it is concluded that applying a jump in the wall temperature is an active method to control the shock wave behavior.

The shock waves filtered contours which are stemmed from the relation $\left(u.\nabla P \Big/ a\sqrt{(P_x^2+P_y^2+P_z^2)}\right)$ are illustrated in Fig. 15, showing the lambda shock wave structure dependency on jumps in the duct wall temperature. The filtration implies that the previous relation is equal to zero when $\left(\sqrt{(P_x^2+P_y^2+P_z^2)}<0.14P_\infty\right)$. As clearly demonstrated in this figure, with an increase in the discontinuity wall temperature from 200 K to 400 K, the distance between two oblique shocks impacting with a bow shock diminishes from 1.24 mm to 0.24 mm. Subsequently, by increasing the discontinuity wall temperature to higher than 400 K, the structure of the shock waves is not lambda anymore, and the oblique shocks merge before the bow shock. As the jump temperature rises from 500K to 700 K, the distance between the locations of the oblique shocks increases from 0.8 to 1.7 mm. The change in the collision position of oblique shocks is due to alteration in boundary layer thickness induced by an increase in the flow temperature. As mentioned before, an increase in temperature will result in a decrease in lambda shock strength.

Conclusion

In this study, the supersonic flow behavior with a series of lambda shock waves in a long duct was examined numerically. In this regard, a comparison was made between various subgrid models by

applying the LES method imbedded in a finite volume code. The obtained results were compared to experimental data reported by Weiss et al. [1]. The results demonstrated that the WMLES model presents a higher accuracy than the other subgrid models. After validating the solution method, the changes in the length of diverging part (while the ratio of outlet area to throat area was kept constant) and the effects of discontinuities in the duct wall temperature (temperature jump) at the locations of shock waves were investigated. It was found that with an increase in the length of the diverging section, the minimum wall pressure reduces, and the maximum Mach number of the flow in the duct rises due to a reduction in divergence angle. Additionally, the position of the lambda shock moves towards the duct throat, and the shock waves strength increases and with an increase in the distance between the first and second lambda shocks. Regarding the temperature jump in duct wall, it is indicated that with an increment of discontinuity temperature, the minimum wall pressure increases and the maximum Mach number decreases. This is followed by a decline in the shock wave strength owing to the effect of temperature on the boundary layer thickness. Furthermore, it is noted that increasing the discontinuity temperature results in reduction of the lambda shock wave strength.

References

[1] A. Weiss, A. Grzona, H. Olivier, Behavior of shock trains in a diverging duct, Experiments in Fluids, 49 (2010) 355-365.
[2] K. Matsuo, Y. Miyazato, H.-D. Kim, Shock train and pseudo-shock phenomena in internal gas flows, Progress in aerospace sciences, 35 (1999) 33-100.
[3] (!!! INVALID CITATION !!! [3, 4]).
[4] K. Xu, J. Chang, W. Zhou, D. Yu, Mechanism and Prediction for Occurrence of Shock-Train Sharp Forward Movement, AIAA Journal, 54 (2016) 1403-1412.
[5] N. Li, J. Chang, D. Yu, W. Bao, Y. Song, Mathematical Model of Shock-Train Path with Complex Background Waves, Journal of Propulsion and Power, 33 (2016) 468-478.
[6] C. Zhang, J. Chang, M. Liu, S. Feng, W. Shi, W. Bao, Effect of heat release on movement characteristics of shock train in an isolator, Acta Astronautica, 133 (2017) 185-194.
[7] S.M. Mousavi, R. Pourabidi, E. Goshtasbi-Rad, Numerical investigation of over expanded flow behavior in a single expansion ramp nozzle, Acta Astronautica, (2018).

[8] C. Wang, C. Cheng, K. Cheng, L. Xue, Unsteady behavior of oblique shock train and boundary layer interactions, Aerospace Science and Technology, 79 (2018) 212-222.
[9] M. Kumar, A. Vaidyanathan, On shock train interaction with cavity oscillations in a confined supersonic flow, Experimental Thermal and Fluid Science, 90 (2018) 260-274.
[10] W.-Y. Su, Y. Chen, F.-R. Zhang, P.-P. Tang, Control of pseudo-shock oscillation in scramjet inlet-isolator using periodical excitation, Acta Astronautica, 143 (2018) 147-154.
[11] L. Vanstone, J. Lingren, N.T. Clemens, Simple Physics-Based Model for the Prediction of Shock-Train Location, Journal of Propulsion and Power, 34 (2018) 1428-1441.
[12] L. Vanstone, J. Lingren, N.T. Clemens, Supersonic Isolator Shock-Train Dynamics: Simple Physics-Based Model for Closed-Loop Control of Shock-Train Location, 2018 AIAA Aerospace Sciences Meeting, American Institute of Aeronautics and Astronautics2018.
[13] W. Shi, J. Chang, J. Zhang, J. Ma, Z. Wang, W. Bao, Numerical investigation on the forced oscillation of shock train in hypersonic inlet with translating cowl, Aerospace Science and Technology, 87 (2019) 311-322.
[14] N. Li, J. Chang, K. Xu, D. Yu, Y. Song, Closed-loop control of shock train in inlet-isolator with incident shocks, Experimental Thermal and Fluid Science, 103 (2019) 355-363.
[15] M. Siavashi, K. Karimi, Q. Xiong, M.H. Doranehgard, Numerical analysis of mixed convection of two-phase non-Newtonian nanofluid flow inside a partially porous square enclosure with a rotating cylinder, Journal of Thermal Analysis and Calorimetry, 137 (2019) 267-287.
[16] M.V. Bozorg, M. Hossein Doranehgard, K. Hong, Q. Xiong, CFD study of heat transfer and fluid flow in a parabolic trough solar receiver with internal annular porous structure and synthetic oil–Al2O3 nanofluid, Renewable Energy, 145 (2020) 2598-2614.
[17] A. Izadi, M. Siavashi, Q. Xiong, Impingement jet hydrogen, air and CuH2O nanofluid cooling of a hot surface covered by porous media with non-uniform input jet velocity, International Journal of Hydrogen Energy, 44 (2019) 15933-15948.
[18] Q. Xiong, S.-C. Kong, High-Resolution Particle-Scale Simulation of Biomass Pyrolysis, ACS Sustainable Chemistry & Engineering, 4 (2016) 5456-5461.
[19] R. Rockwell, C.P. Goyne, L. Di, Z. Lin, R. Bakos, J.M. Donbar, Simulated Shock Train Control using an All-Coefficient Adaptive Control Approach, AIAA Scitech 2019 Forum, American Institute of Aeronautics and Astronautics2019.
[20] S.M. Mousavi, J. Abolfazli-Esfahani, M. Yazdi-Mamaghani, Numerical study of entropy generation in the flameless oxidation using large eddy simulation model and OpenFOAM software, International Journal of Thermodynamics, 17 (2014) 202-208.
[21] S.M. Mousavi, J. Abolfazli-Esfahani, Numerical Investigation of the Flameless Oxidation of Natural Gas in the IFRF Furnace Using Large Eddy Simulation, International Journal of Spray and Combustion Dynamics, 6 (2014) 387-410.
[22] R. Kamali, S.M. Mousavi, A.R. Binesh, J. Abolfazli-Esfahani, Large eddy simulation of the flameless oxidation in the IFRF furnace with varying inlet conditions, International Journal of Spray and Combustion Dynamics, 9 (2016) 102-115.
[23] C. Fureby, A Large Eddy Simulation (LES) Study of the VOLVO and AFRL Bluff Body Combustors at Different Operating Conditions, AIAA Scitech 2019 Forum, American Institute of Aeronautics and Astronautics2019.
[24] A. Triantafyllidis, E. Mastorakos, Spark ignition and expansion of a turbulent non-premixed bluff-body methane flame using Large Eddy Simulations, 49th AIAA Aerospace Sciences Meeting including the New Horizons Forum and Aerospace Exposition, American Institute of Aeronautics and Astronautics2011.

[25] J.W. Foster, R.S. Miller, Survey of Turbulent Combustion Models for Large-Eddy Simulations of Propulsive Flowfields, 53rd AIAA Aerospace Sciences Meeting, American Institute of Aeronautics and Astronautics2015.
[26] K. Makowka, N.C. Dröske, J. von Wolfersdorf, T. Sattelmayer, Hybrid RANS/LES of a supersonic combustor, Aerospace Science and Technology, 69 (2017) 563-573.
[27] H. Pitsch, Large-eddy simulation of turbulent combustion, Annu. Rev. Fluid Mech., 38 (2006) 453-482.
[28] L.A. Martínez-Tossas, M.J. Churchfield, C. Meneveau, Large Eddy Simulation of wind turbine wakes: detailed comparisons of two codes focusing on effects of numerics and subgrid modeling, Journal of Physics: Conference Series, 625 (2015) 012024.
[29] C. Wagner, T. Hüttl, P. Sagaut, Large-eddy simulation for acoustics, Cambridge University Press2007.
[30] S.A. Karabasov, M.Z. Afsar, T.P. Hynes, A.P. Dowling, W.A. McMullan, C.D. Pokora, G.J. Page, J.J. McGuirk, Jet Noise: Acoustic Analogy informed by Large Eddy Simulation, AIAA Journal, 48 (2010) 1312-1325.
[31] Y. Addad, D. Laurence, C. Talotte, M.C. Jacob, Large eddy simulation of a forward-backward facing step for acoustic source identification, in: W. Rodi, N. Fueyo (Eds.) Engineering Turbulence Modelling and Experiments 5, Elsevier Science Ltd, Oxford, 2002, pp. 719-728.
[32] T. Nonomura, H. Nakano, Y. Ozawa, D. Terakado, M. Yamamoto, K. Fujii, A. Oyama, Large eddy simulation of acoustic waves generated from a hot supersonic jet, Shock Waves, (2019).
[33] A. Fattahi, S.M. Hosseinalipour, N. Karimi, On the dissipation and dispersion of entropy waves in heat transferring channel flows, Physics of Fluids, 29 (2017) 087104.
[34] A. Fattahi, S.M. Hosseinalipour, N. Karimi, Z. Saboohi, F. Ommi, On the response of a lean-premixed hydrogen combustor to acoustic and dissipative-dispersive entropy waves, Energy, 180 (2019) 272-291.
[35] M.S. Loginov, N.A. Adams, A.A. Zheltovodov, LES of Shock Wave/Turbulent Boundary Layer Interaction, in: E. Krause, W. Jäger, M. Resch (Eds.) High Performance Computing in Science and Engineering' 04, Springer Berlin Heidelberg, Berlin, Heidelberg, 2005, pp. 177-188.
[36] W. Li, H. Liu, Large-eddy simulation of shock-wave/boundary-layer interaction control using a backward facing step, Aerospace Science and Technology, 84 (2019) 1011-1019.
[37] H. Koo, V. Raman, Large-Eddy Simulation of a Supersonic Inlet-Isolator, AIAA Journal, 50 (2012) 1596-1613.
[38] Z.P. Vane, S.K. Lele, Simulations of a Normal Shock Train in a Constant Area Duct Using Wall-Modeled LES, 43rd Fluid Dynamics Conference, American Institute of Aeronautics and Astronautics2013.
[39] J.F. Quaatz, M. Giglmaier, S. Hickel, N.A. Adams, Large-eddy simulation of a pseudo-shock system in a Laval nozzle, International Journal of Heat and Fluid Flow, 49 (2014) 108-115.
[40] B. Morgan, K. Duraisamy, S.K. Lele, Large-Eddy Simulations of a Normal Shock Train in a Constant-Area Isolator, AIAA Journal, 52 (2014) 539-558.
[41] S.M. Mousavi, E. Roohi, Three dimensional investigation of the shock train structure in a convergent–divergent nozzle, Acta Astronautica, 105 (2014) 117-127.
[42] R. Kamali, S.M. Mousavi, A.R. Binesh, Three dimensional CFD investigation of shock train structure in a supersonic nozzle, Acta Astronautica, 116 (2015) 56-67.
[43] R. Kamali, S.M. Mousavi, D. Khojasteh, Three-Dimensional Passive and Active Control Methods of Shock Wave Train Physics in a Duct, International Journal of Applied Mechanics, 08 (2016) 1650047.

[44] S.M. Mousavi, E. Roohi, Large eddy simulation of shock train in a convergent–divergent nozzle, International Journal of Modern Physics C, 25 (2014) 1450003.
[45] E. Goshtasbi Rad, S.M. Mousavi, Wall modeled large eddy simulation of supersonic flow physics over compression–expansion ramp, Acta Astronautica, 117 (2015) 197-208.
[46] S. Mahapatra, S. Kumar, K.P. Sinhamahapatra, S. Ghosh, Large-eddy simulation of shock-turbulence interaction in supersonic diffuser flows, Journal of Turbulence, 18 (2017) 512-538.
[47] M.S.H. Joy, A.B.M.T. Hasan, Large eddy simulation of shock train phenomena in a gas dynamic flow passage, AIP Conference Proceedings, 1980 (2018) 040009.
[48] J. Allen, T. Hauser, C.J. Tam, Numerical Simulations of a Scramjet Isolator Using RANS and LES Approaches, 45th AIAA Aerospace Sciences Meeting and Exhibit, American Institute of Aeronautics and Astronautics2007.
[49] J. Smagorinsky, General circulation experiments with the primitive equations: I. The basic experiment, Monthly weather review, 91 (1963) 99-164.
[50] J.W. Deardorff, A numerical study of three-dimensional turbulent channel flow at large Reynolds numbers, Journal of Fluid Mechanics, 41 (1970) 453-480.
[51] C. Fureby, F.F. Grinstein, Large Eddy Simulation of High-Reynolds-Number Free and Wall-Bounded Flows, Journal of Computational Physics, 181 (2002) 68-97.
[52] S. Kawai, J. Larsson, Wall-modeling in large eddy simulation: Length scales, grid resolution, and accuracy, Physics of Fluids, 24 (2012) 015105.
[53] F. Nicoud, F. Ducros, Subgrid-Scale Stress Modelling Based on the Square of the Velocity Gradient Tensor, Flow, Turbulence and Combustion, 62 (1999) 183-200.
[54] M.L. Shur, P.R. Spalart, M.K. Strelets, A.K. Travin, A hybrid RANS-LES approach with delayed-DES and wall-modelled LES capabilities, International Journal of Heat and Fluid Flow, 29 (2008) 1638-1649.
[55] J. Fröhlich, D. von Terzi, Hybrid LES/RANS methods for the simulation of turbulent flows, Progress in Aerospace Sciences, 44 (2008) 349-377.
[56] M. Keating, A. Principal Engineer, Accelerating CFD solutions, advantage, 1 (2011) 48.
[57] T. Barth, D. Jespersen, The design and application of upwind schemes on unstructured meshes, 27th Aerospace Sciences Meeting, American Institute of Aeronautics and Astronautics1989.
[58] T.J. Chung, Computational Fluid Dynamics, Cambridge University Press, Cambridge, 2015.
[59] S.B. Pope, Turbulent Flows, Cambridge University Press, Cambridge, 2000.
[60] F.K. Chow, R.L. Street, M. Xue, J.H. Ferziger, Explicit Filtering and Reconstruction Turbulence Modeling for Large-Eddy Simulation of Neutral Boundary Layer Flow, Journal of the Atmospheric Sciences, 62 (2005) 2058-2077.
[61] W. Langhans, J. Schmidli, B. Szintai, A Smagorinsky-Lilly turbulence closure for COSMO-LES: Implementation and comparison to ARPS, COSMO newsletter, 12 (2012) 20-31.

List of figures

Fig. 1.	A schematic representation of duct geometry.
Fig. 2.	Configuration of 3D cells at different locations of the computational domain.
Fig. 3.	Comparison between the obtained results of three subgrid models and the experimental data reported by Ref. [1].
Fig. 4.	Comparison between the real shocks structure and WMLES results. Experimental images were taken from Ref. [1].
Fig. 5.	Contours of instantaneous stagnation pressure and pressure gradient.
Fig. 6.	Distribution of instantaneous stagnation pressure
Fig. 7.	Distribution of wall pressure at various divergence section length.
Fig. 8.	Distribution of Mach number at various divergence section length
Fig. 9.	Variation in boundary layer thickness at various divergence section length
Fig. 10.	Pressure gradient contours at various diverging section length
Fig. 11.	Mach number contours at various lengths of diverging section such as a- 0.56 m, b- 0.58, c- 0.6, d- 0.62, and e-0.64.
Fig. 12.	Wall pressure distribution at various wall temperatures.
Fig. 13.	Reynolds number distribution at various wall temperatures.
Fig. 14.	Mach number distribution at various wall temperatures.
Fig. 15.	Filtered shock waves contours at various wall temperatures.

List of tables

Table 1.	Boundary condition according to Ref. [1].
Table 2.	Minimum pressure and maximum Mach number dependency on the divergence length

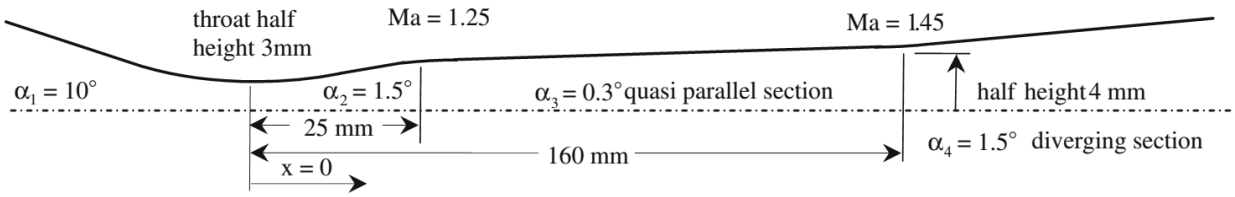

Fig. 1. A schematic representation of duct geometry.

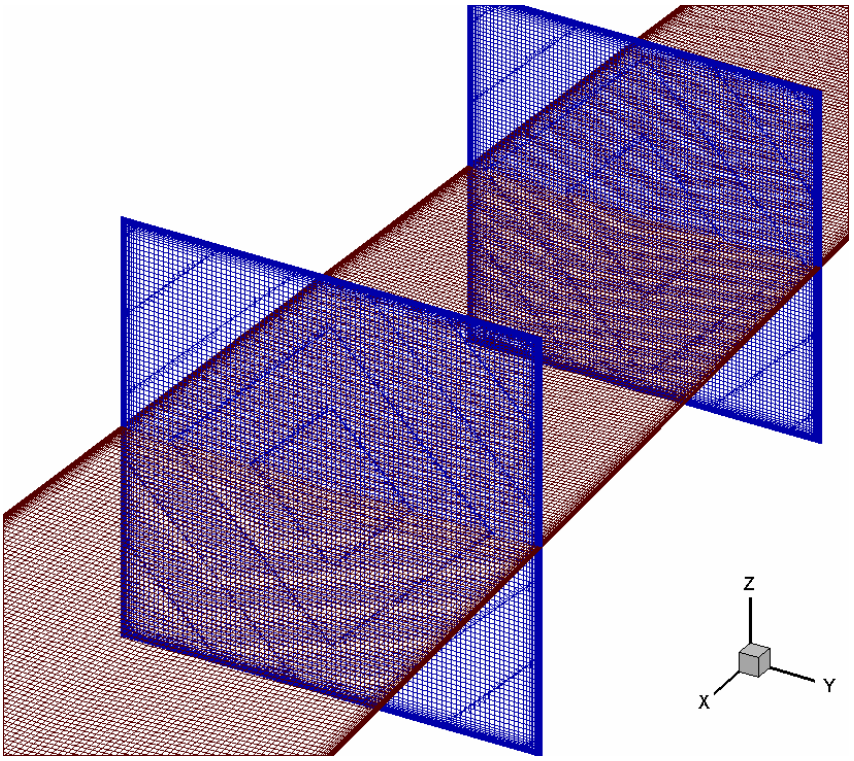

Fig. 2. Configuration of 3D cells at different locations of the computational domain.

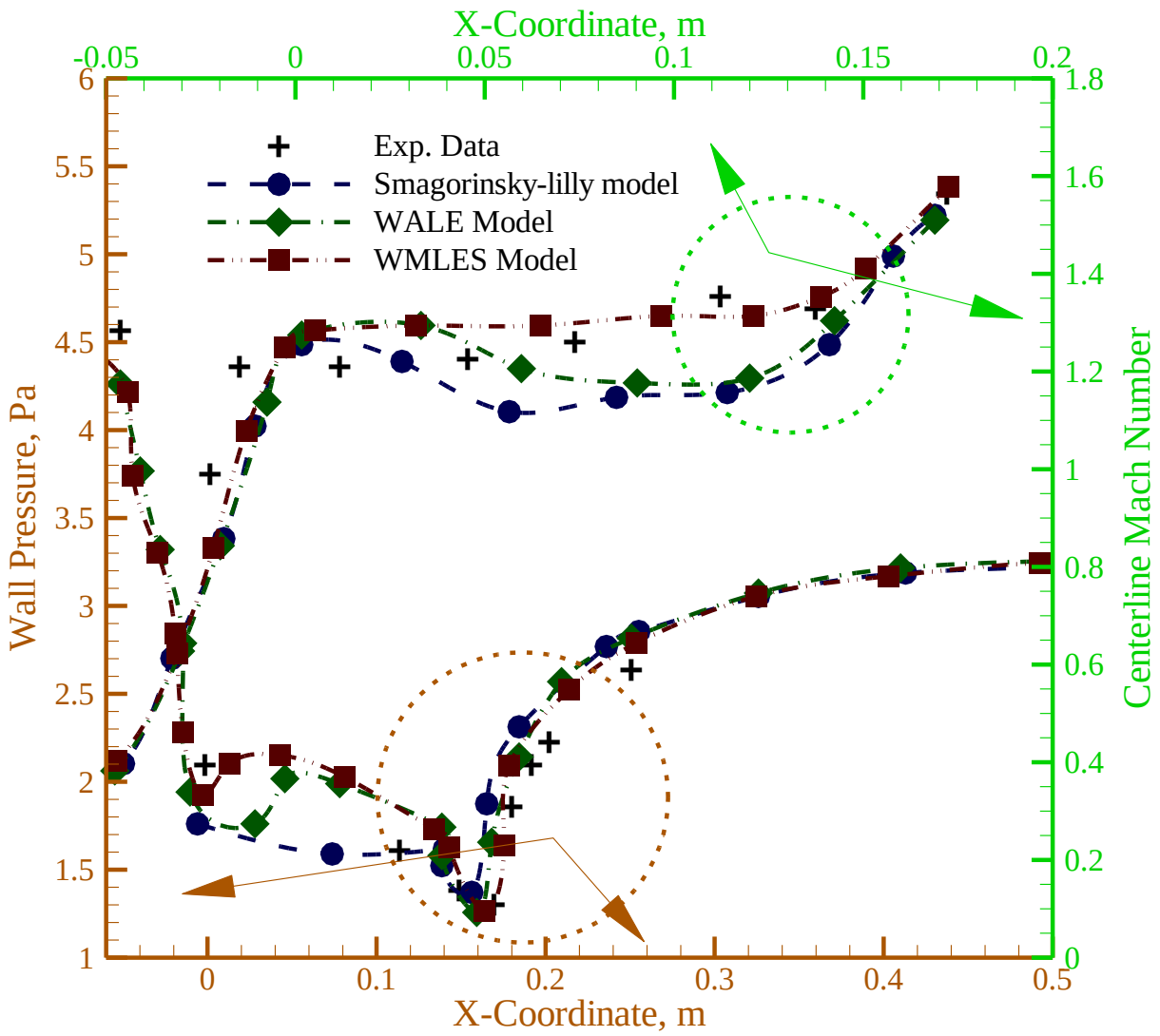

Fig. 3. Comparison between the obtained results of three subgrid models and the experimental data reported by Ref. [1].

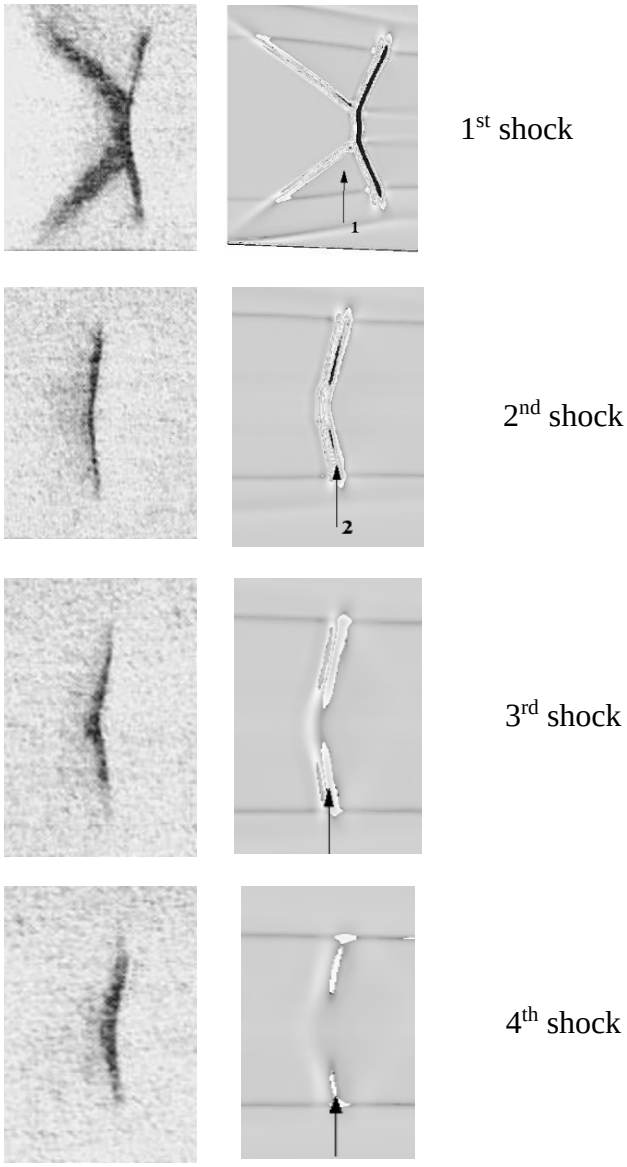

Fig. 4. Comparison between the real shocks structure and WMLES results. Experimental images were taken from Ref. [1].

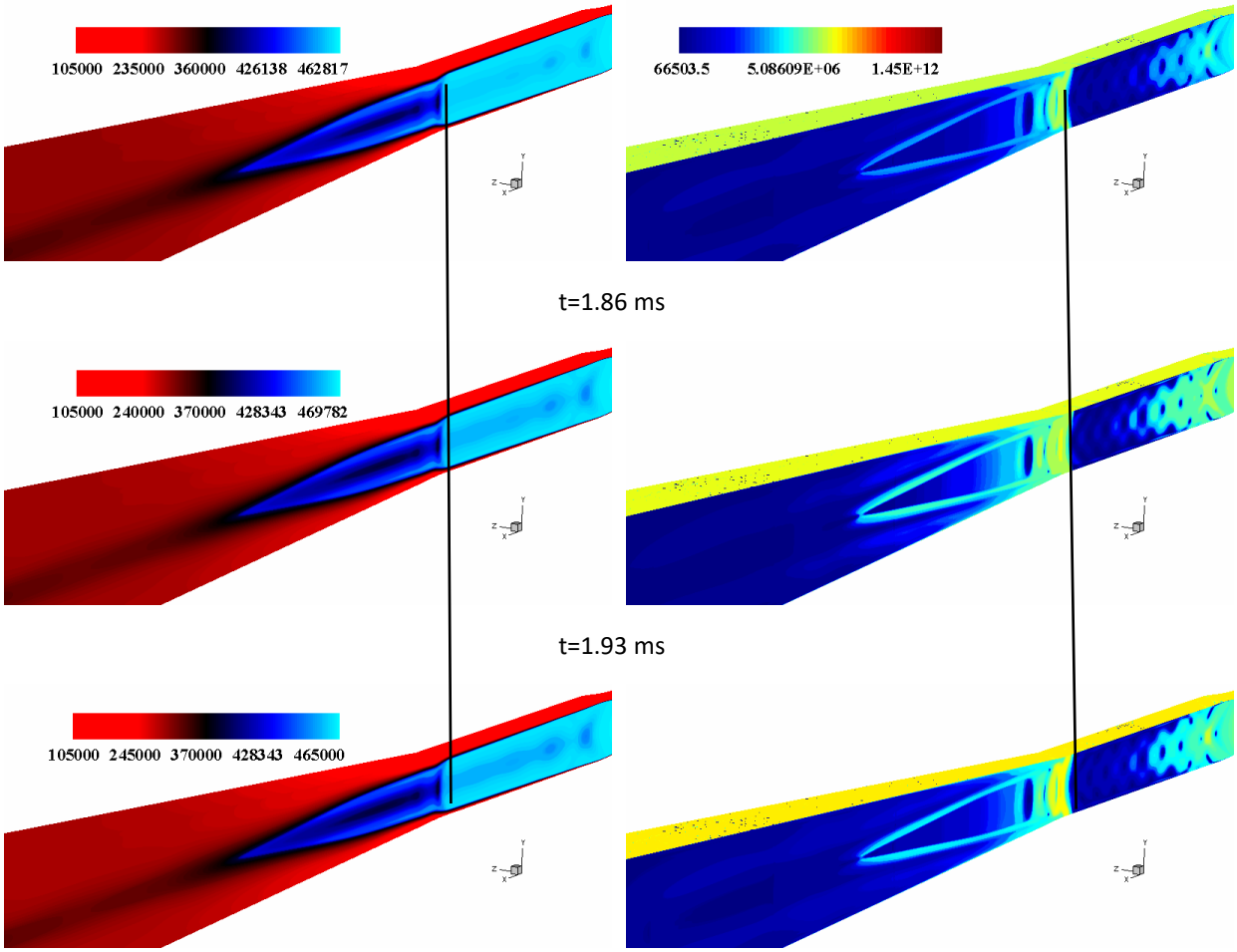

Fig. 5. Contours of instantaneous stagnation pressure and pressure gradient.

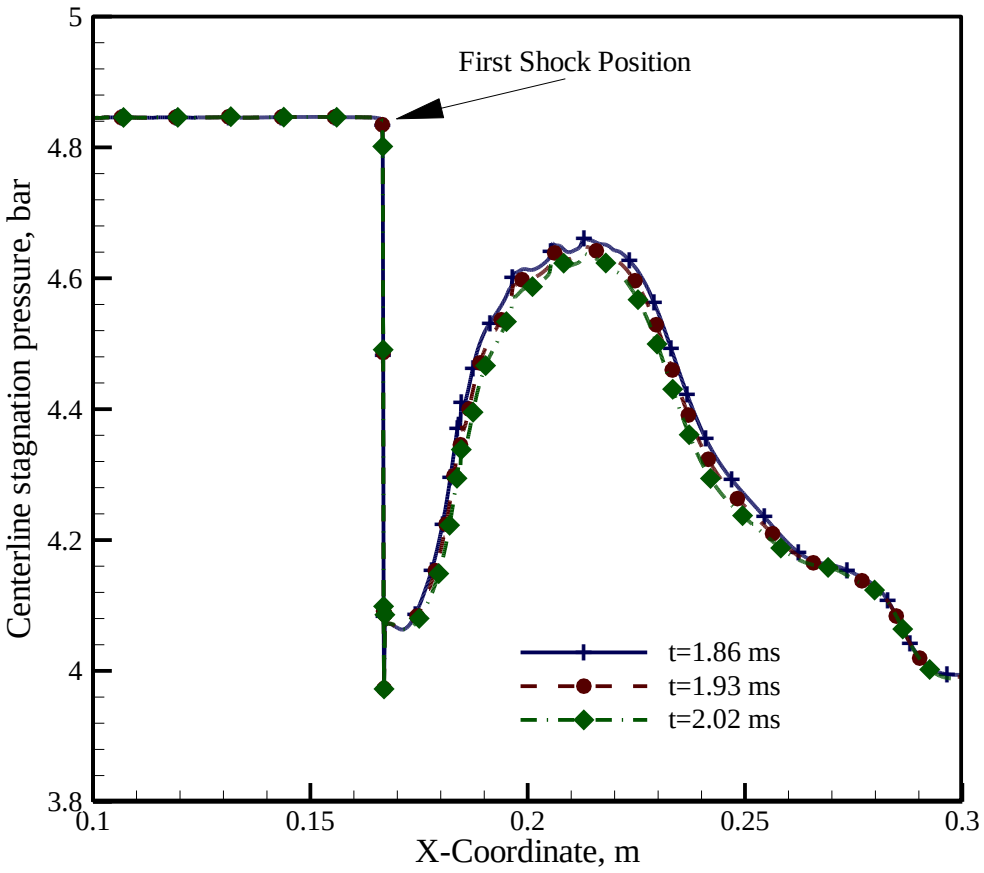

Fig. 6. Distribution of instantaneous stagnation pressure

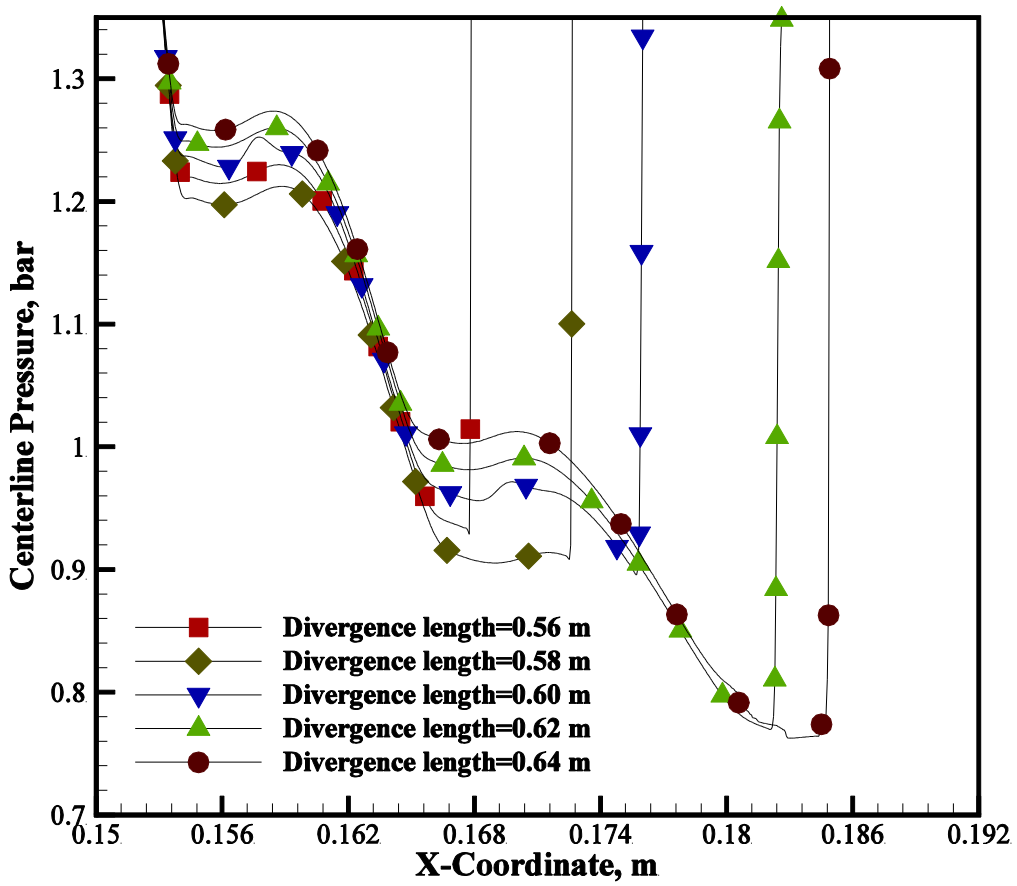

Fig. 7. Distribution of wall pressure at various divergence section length.

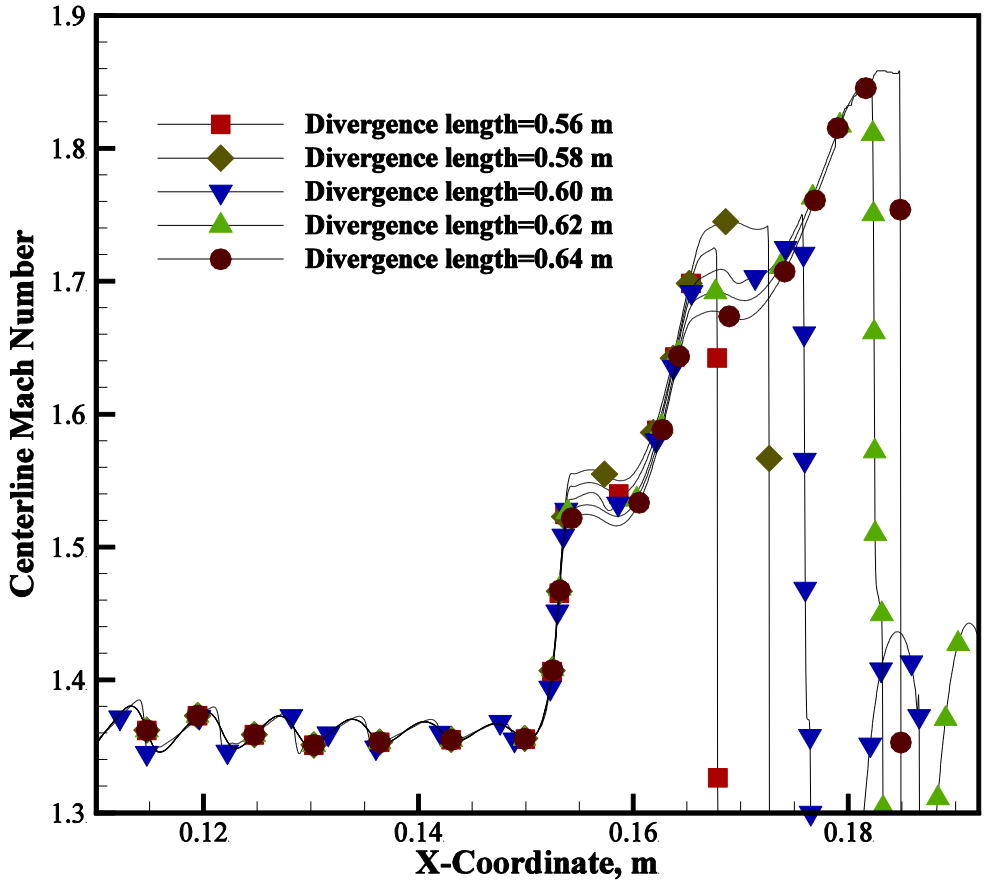

Fig. 8. Distribution of Mach number at various divergence section length.

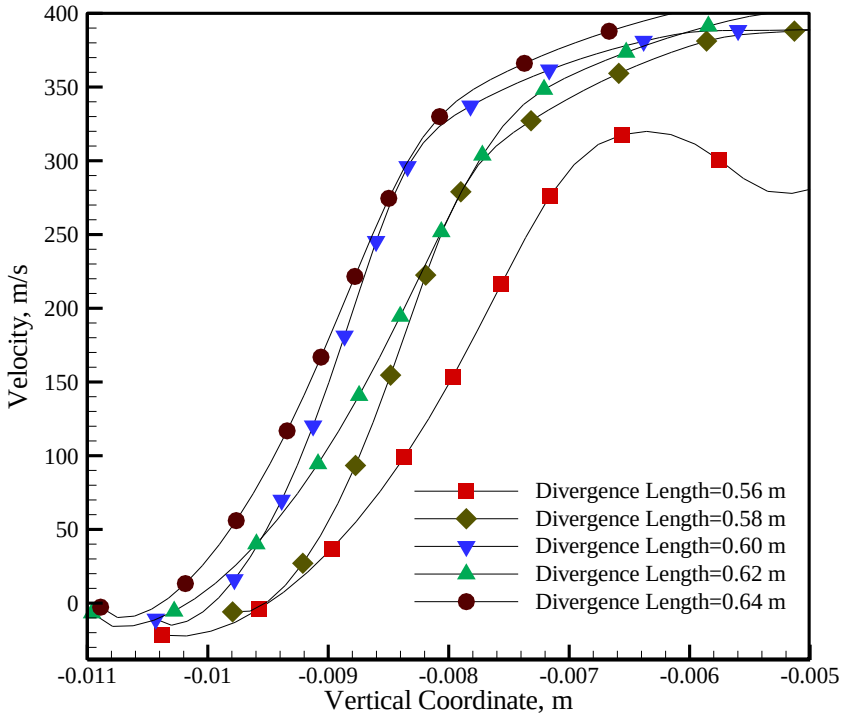

Fig. 9. Variation in boundary layer thickness at various divergence section length

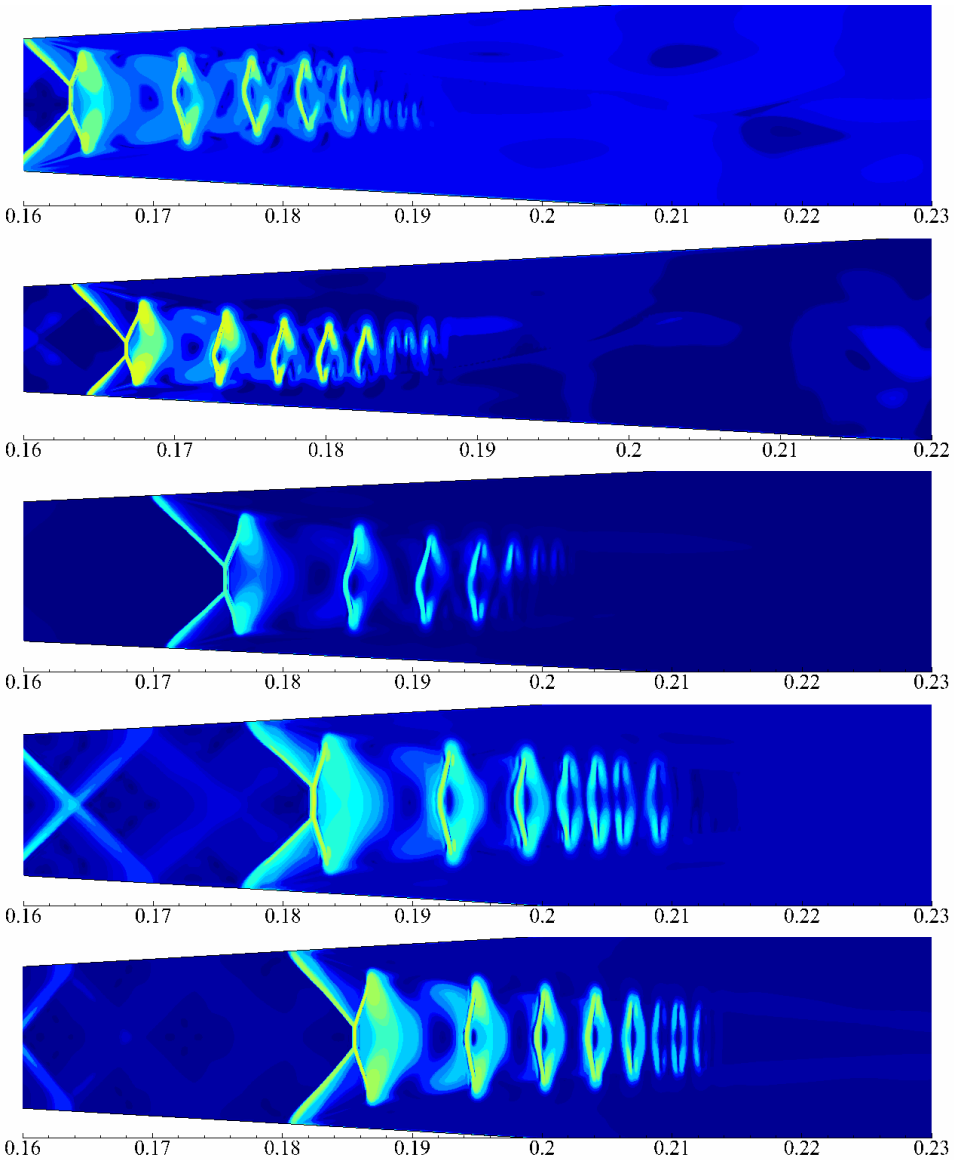

Fig. 10. Pressure gradient contours at various diverging section length.

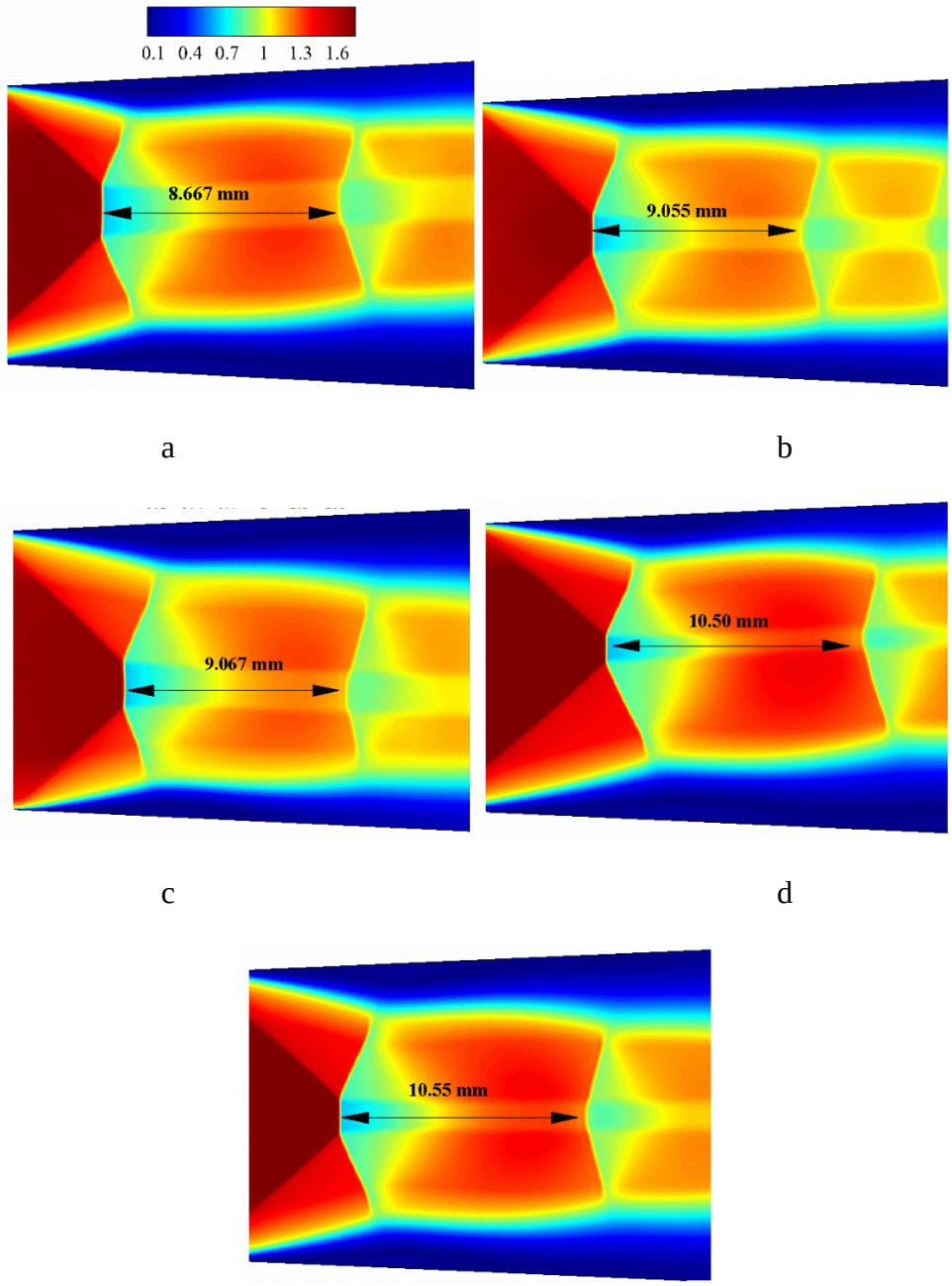

Fig. 11. Mach number contours at various lengths of diverging section such as a- 0.56 m, b- 0.58, c- 0.6, d- 0.62, and e-0.64.

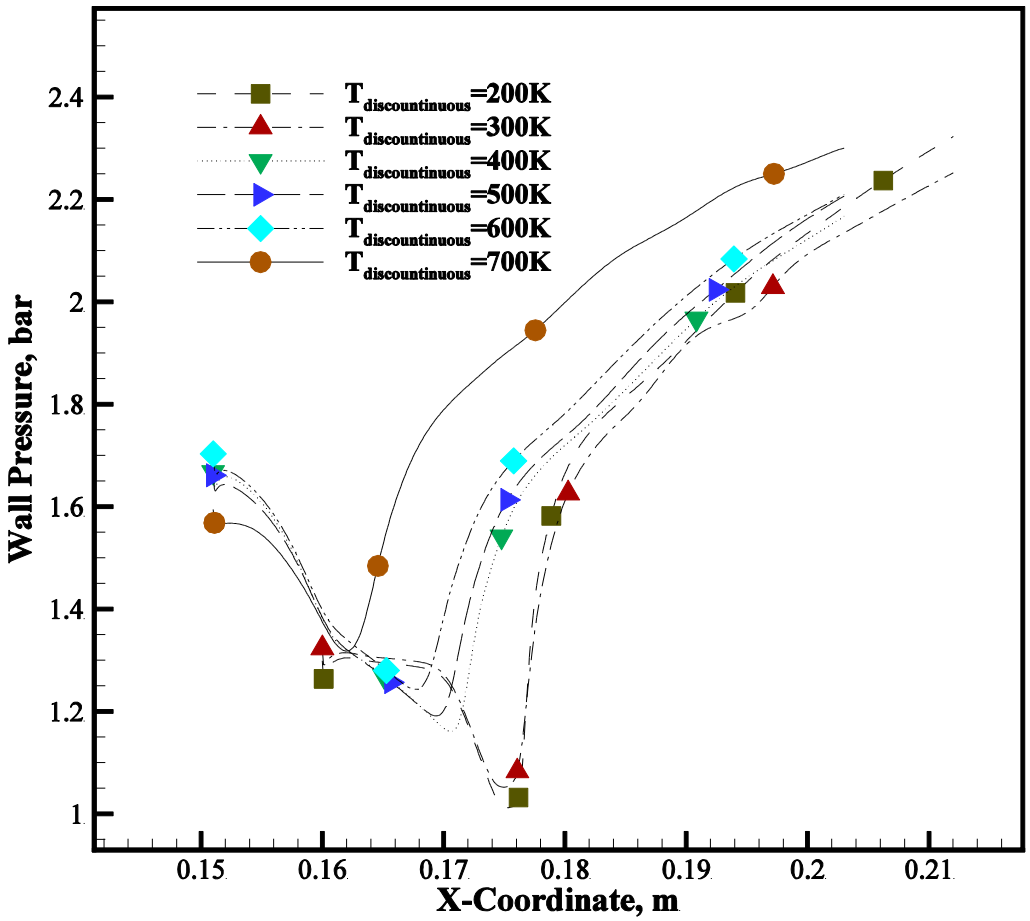

Fig. 12. Wall pressure distribution at various wall temperatures.

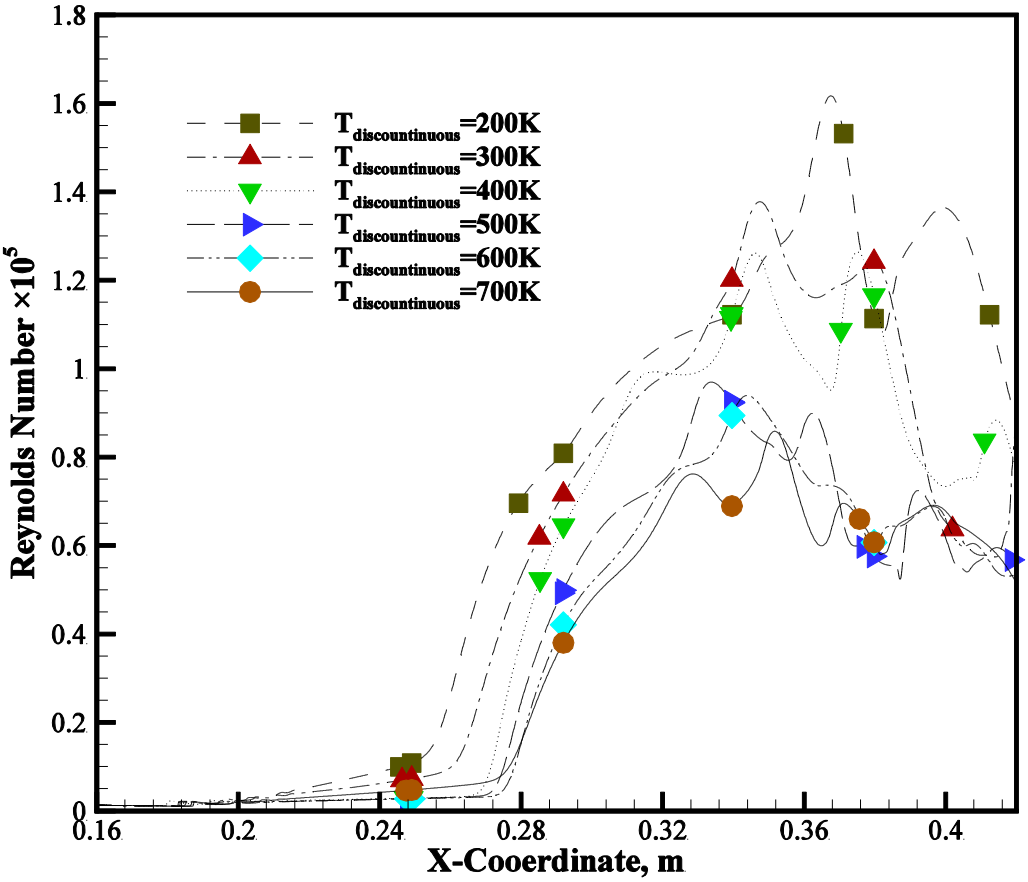

Fig. 13. Reynolds number distribution at various wall temperatures.

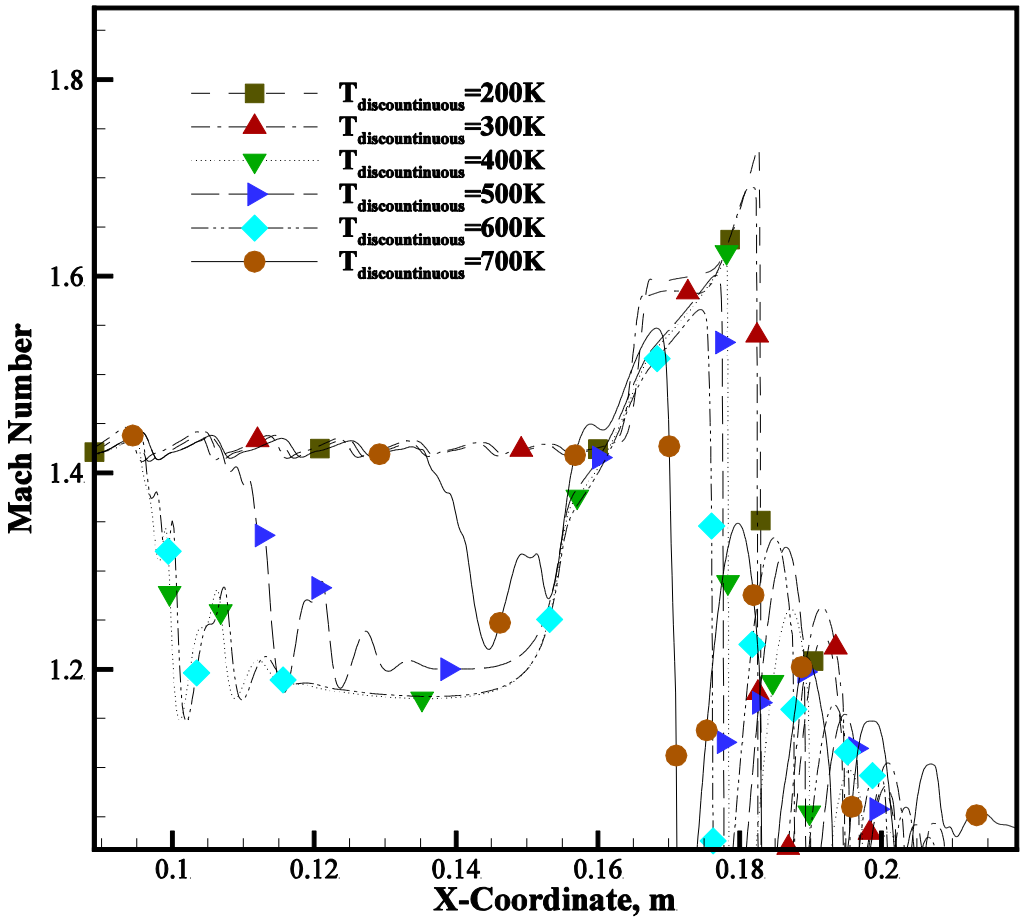

Fig. 14. Mach number distribution at various wall temperatures.

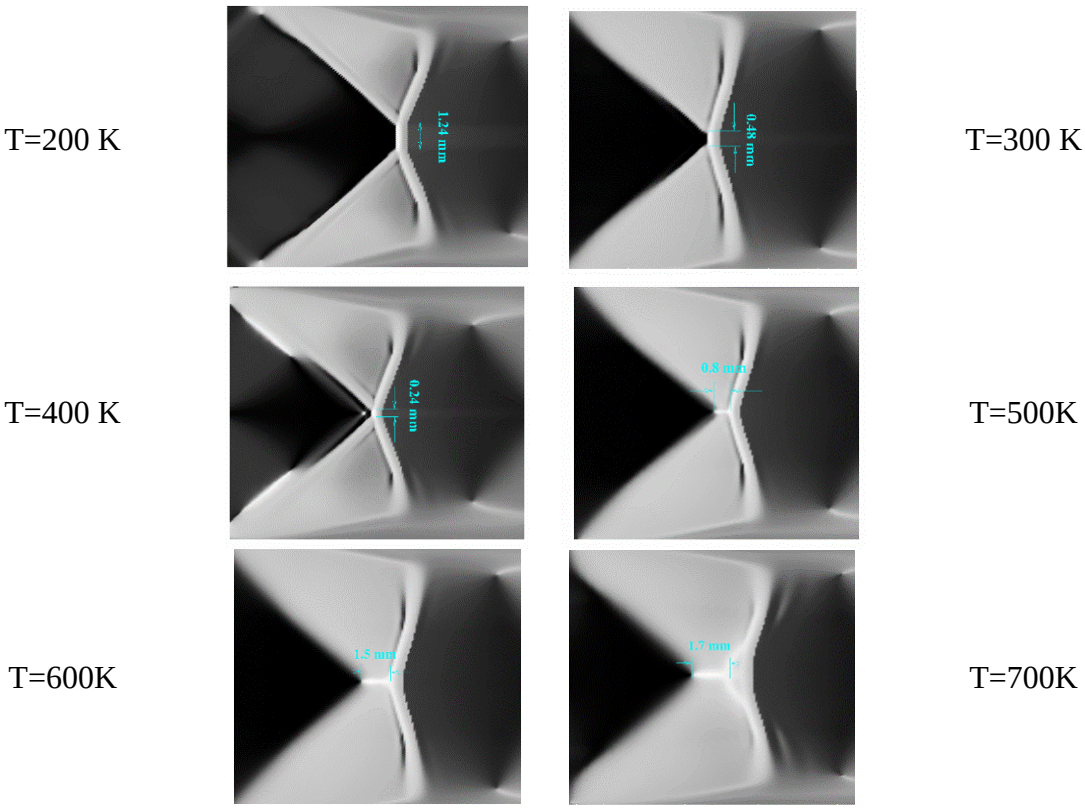

Fig. 15. Filtered shock waves contours at various wall temperatures.

Table 1. Boundary condition according to Ref. [1].

	P_{total} (kPa)	P_{static} (kPa)	T (K)	V ($m.s^{-1}$)
Inlet	480	-	300	89.27
Outlet	-	325	-	-

Table 2. Boundary condition for turbulent characteristics.

Backflow turbulent intensity (%)	3.4
Backflow hydraulic diameter (m)	0.047
Backflow UU Reynolds stress (m^2/s^2)	1
Backflow VV Reynolds stress (m^2/s^2)	1
Backflow WW Reynolds stress (m^2/s^2)	1
Backflow UV Reynolds stress (m^2/s^2)	0
Backflow VW Reynolds stress (m^2/s^2)	0
Backflow UW Reynolds stress (m^2/s^2)	0

Table 3. Minimum pressure and maximum Mach number dependency on the divergence length.

Diverging length, m	0.56	0.58	0.6	0.62	0.64
P_{min}	0.94	0.91	0.89	0.79	0.78
M_{max}	1.71	1.72	1.725	1.86	1.88